sustainability

MDPI

Article

Experimental Study on the Shear Performance of Reinforced Concrete Beams Strengthened with Bolted Side-Plating

Xin Liu [1], Yu Chen [1], Ling-Zhi Li [1,*], Mei-Ni Su [2], Zhou-Dao Lu [1] and Ke-Quan Yu [3]

[1] Department of Disaster Mitigation for Structures, College of Civil Engineering, Tongji University, 1239 Siping Road, Shanghai 200092, China; lx900314@126.com (X.L.); tongjichenyu@163.com (Y.C.); lzd@tongji.edu.cn (Z.-D.L.)

[2] School of Mechanical, Aerospace and Civil Engineering, University of Manchester, Manchester M1 3NJ, UK; meini.su@manchester.ac.uk

[3] School of Engineering and Information Technology, The University of New South Wales, Sydney, NSW 2052, Australia; Kequan.yu@adfa.edu.au

* Correspondence: tjlilingzhi@gmail.com; Tel.: +86-21-6598-1431

Received: 29 March 2019; Accepted: 17 April 2019; Published: 26 April 2019

Abstract: To investigate the residual shear capacity of post-fire bolted side-plated (BSP) reinforced concrete (RC) beams with different depths of steel plate and types of anchor adhesive, i.e., magnesium oxychloride cement (MOC) and HIT-RE500, a control beam and five BSP beams were fabricated, of which two were exposed to fire in accordance with ISO834 temperature curve. Four-point bending shear tests were conducted to investigate the influence of elevated temperature on the failure mode, cracking load, shear capacity, stiffness, ductility and strain development, etc. The shear capacities of RC beams were found to be improved significantly by using the BSP technique. However, the stiffness of BSP beams was seriously degraded after exposed to fire, but the reduction in shear capacity was negligible, whereas the ductility and the strain of longitudinal reinforcement were obviously increased. Thus, the failure-mode was changed from shear failure to flexural failure. Regarding the adhesive mortar used for bolt anchorage, magnesium oxychloride cement (MOC) achieved higher shear capacity and better ductility but lower stiffness for BSP beams compared with HIT-RE500. Additionally, increasing the depth of bolted steel plates effectively improved the shear performance of BSP beams. In the tests, uneven relative slips were observed on the plate-RC interface due to the shear deformation of bolt shafts and the plates' tensile principal stress perpendicular to the main diagonal crack, which proved the deformation lag of the bolted steel plates with respect to the RC beam. The outcomes of this study provide a better understanding on the shear performance of BSP beams at room temperatures and at fire conditions.

Keywords: reinforced concrete beam; bolted side-plating; exposed to fire; shear performance; magnesium oxychloride cement

1. Introduction

Comprehensive methods can be employed to increase the bear capacity of reinforced concrete (RC) structures, such as structural retrofitting [1–4] and the use of high-performance materials [5–15]. Recently, a newly arising bolted side-plating (BSP) technique, i.e., attaching steel plates to the side faces of reinforced concrete (RC) beams using anchor bolts, has become increasingly popular all over the world [16–19]. The BSP technique not only has the advantages such as minimal space occupation and easy installation, but also avoids serious debonding and peeling failures that are common in RC beams strengthened by adhesively bonded steel plates [20] or fibre-reinforced polymers (FRP) [21–25].

A variety of theoretical and experimental studies have been conducted to investigate the strengthening effects and mechanical behaviours of BSP beams. Oehlers et al. [26] established the relationship between the degree of transverse partial interaction and the properties of anchor bolts. Based on this model, Nguyen et al. [27] derived the relationship between longitudinal and transverse partial interactions as well as the distribution of slip strain, slip and neutral-axis separation. Su et al. [28–30] conducted experimental and numerical studies on BSP beams, which showed that even small slips on the steel-concrete interface could significantly affect the overall response. Su and Siu [31–33] proposed numerical procedures for predicting the nonlinear load-deformation response of bolt groups as well as the longitudinal and transverse slip in BSP beams. Li et al. [34–40] conducted comprehensive experimental, numerical and theoretical studies on the BSP technique, and found that the flexural strength, shear strength, stiffness and ductility of RC beams could be effectively improved. All studies show that the BSP method is feasible and effective to rehabilitate RC beams in existing buildings and infrastructures.

However, most existing studies are focused on the flexural performance of BSP beams, studies on the shear behaviour are still limited: Barnes et al. [41] compared the shear strengthening effect of fixing steel plates to the side faces of RC beams by using adhesive bonding or bolting. Su and Zhu [28] investigated the shear performance of BSP-strengthened coupling beams and found that small uneven slips on the steel–concrete interface would cause serious loss in shear strengthening effect. Su and Cheng [16] investigated the shear performance of coupling beams retrofitted by bolted steel plates with or without buckling restraining device, and considerable improvement in deformability and energy dissipation were found. Li et al. [42,43] conducted an experimental study on BSP beams to investigate the shear strengthening effect under the room temperature and proposed a simplified analytical model based on the force equilibrium and deformation compatibility of the beam segment in the shear span.

Furthermore, available research outcomes in the literature have mainly focused on the mechanical behaviour of BSP beams under room temperature; the fire resistance and the post-fire residual capacities have not yet been studied comprehensively. However, building fire is one of the most frequent and threatening disasters for building structures. For instance, the total number of fires reported in UK was 212,500 in the year 2013, 19% of which happened in dwelling buildings [44]. Moreover, Jiang and Li [45,46] have found that the fire exposure can influence the bearing capacity, the stiffness, the ductility factor, and the energy dissipation capacity of the RC structures to a large extent. Thus, the fire resistance of the retrofitted structures should always be paid attention to. Compared to conventional RC beams, the influence of fire on BSP beams is far more complex, which might affect concrete, steel plates, steel bars, anchor bolts, and adhesive mortar for bolt anchorage. Therefore, the fire resistance and post-fire performance of BSP beams are highly dependent on the coupling effects of all the components. Arioz [47] and Kodur [48] studied the effect of fire on the mechanical properties of concrete, such as density, compressive strength, and modulus of elasticity. Kadhum [49] found that with increasing temperature, the strength, ductility and stiffness of concrete were progressively reduced, and the crack width increased. Topcu and Unluoglu [50–53] found that the post-fire yield and ultimate strengths of rebars decreased when the temperature goes up. Ergun and Kurklu [54] found that the residual bond strength between reinforcing bar and concrete decreased with increasing temperature. Since the steel plates in BSP beams are directly exposed to fire, the effect of fire on steel material and the possible fire protection measures are of the greatest importance. Li et al. [55] conducted experimental studies on the high-temperature properties of two kinds of constructional steel widely used in China. Miamis [56], Kwon and Shin [57] found that the ductility of steel increased with elevated temperature, but the yield and tensile strengths, modulus of elasticity, and elongation decreased with the elevated temperature. Santiago et al. [58] proposed that the yield strength of anchor bolts decreased and the ductility increased significantly after the temperature was higher than 500 °C. Kirby [59] found that the behaviour of high-strength Grade 8.8 bolts highlighted a marked loss in the ultimate capacity at elevated temperatures between 300 and 700 °C.

Since the bolting connection has a dominant effect in the performance of BSP beams, the adhesive mortar used for bolt anchorage is of great importance for the BSP technique. Banea and Sousa [60] found that the ultimate tensile stress of epoxy adhesive decreased linearly as the temperature keeps increasing. The glass transition temperature of the epoxy adhesive is approximately 155 °C, which reflects the poor fire resistance of epoxy adhesive. On the other hand, magnesium oxychloride cement (MOC) is widely used in fireproof materials and thermal insulation materials due to its advantageous characteristics such as high fire resistance, low thermal conductivity, flame retardant activity and good bonding performance [61]. The mechanical properties, compositions, and manufacture of the MOC have also been studied comprehensively [62–64]. In view of the admirable fire-resisting properties of the MOC, it can be selected as the anchor adhesive mortar of the BSP beams to prevent the premature anchorage failure during and after fire exposure.

Existing researches on the behaviour of BSP beams mainly concentrate on their flexural performance at ambient temperature, and very little work has been done on the shear performance, especially for BSP beams after fire. In light of this situation, an experimental study was conducted including fire tests and post-fire shear tests for several BSP beams in the present study, which aims to investigate the post-fire residual shear performance of BSP beams. Thus, the influence of elevated temperature, types of anchor adhesive, and the depth of steel plates on the failure mode, cracking load, shear capacity, stiffness, ductility, strain development, and relative slips on the plate-RC interface were investigated in detail.

2. Experimental Program

2.1. Specimen Details

A total of six RC beams were casted with a length of 2600 mm, a cross-section of 200 mm × 400 mm, and a concrete cover of 30 mm considering the size of the furnace and the designed shear span ratio. Figure 1a shows the dimensions and the reinforcement details of the RC beams. The notations 'T' and 'R' denote the high-yield deformed steel bars and the mild steel round bars, respectively. Compressive reinforcement of 2T12, tensile reinforcement of 3T25, and transverse reinforcement of R6-200 were used for all specimens. To ensure the specimens to fail by shear, the tensile reinforcement ratio was designed as 2.1% and the shear reinforcement ratio was 1.0%.

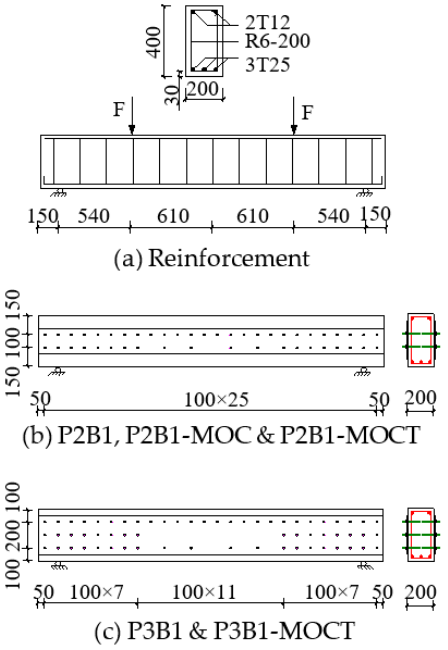

Figure 1. Reinforcement and strengthening details (dimensions in mm).

Table 1 summarises the name and design parameters of all specimens. CTRL was a control beam without any retrofitting. The other five were retrofitted using the BSP technique, of which two BSP beams were exposed to fire. Figure 1b,c shows the layout of steel plates and anchor bolts of all BSP specimens. Steel plates with a thickness of 4 mm, a length of 2600 mm and two depths of 200 mm and 300 mm were used for BSP beams. A bolt spacing of 100 mm and two kinds of adhesive mortar (HIT-RE 500 and MOC) were employed for the post-installed bolt anchoring system. All BSP beams were named in accordance with the strengthening parameters. The letter "P" and the following number represent the depth of steel plates in decimeters, the letter "B" and the subsequent number represent the bolt spacing in decimeters, while the letters "MOC" means the BSP beams were anchored by MOC adhesive mortar and "T" indicates the specimens were tested after being exposed to fire.

Table 1. Design parameters of specimens.

Specimen	Plate Depth (mm)	Bolt Spacing (mm)	Anchor Adhesive Mortar	Temperature Environment
CTRL	N/A	N/A	N/A	N/A
P2B1	200	100	HIT-RE500	Room Temperature
P3B1	300	100	HIT-RE500	Room Temperature
P2B1-MOC	200	100	MOC	Room Temperature
P2B1-MOCT	200	100	MOC	High Temperature
P3B1-MOCT	300	100	MOC	High Temperature

Additionally, the number and the horizon spacing of the anchor bolts decreased in the pure bending zone, because in this area, both the transfer of shear and longitudinal stress between the bolted steel plates and the RC beams were fairly low, thus fewer anchor bolts were needed.

2.2. Material Properties

Nine concrete cubes of 150 mm × 150 mm were casted to conduct the compressive tests, and the average compressive strength was found to be 61.5 MPa. Three steel bar samples with a length of 500 mm and three coupon samples with dimensions of 230 mm × 20 mm taken from steel plates were tested to get the yield strength, ultimate strength and Young's modulus, as shown in Table 2.

Table 2. Mechanical properties of reinforcements and steel plates.

Sample	Diameter/Thickness (mm)	Yield Strength (MPa)	Ultimate Strength (MPa)	Young's Modulus (GPa)
Shear stirrup	6	574	675	219
Compressive rebar	12	484	628	184
Tensile rebar	25	471	636	194
Steel plate	4	324	469	209
Anchor bolt	12	689	810	211

The anchor bolts were Grade 8.8, with a Young's modulus of 211 GPa, a yield strength of 686 MPa, and an ultimate strength of 810MPa. The HIT-RE500 adhesive mortar produced by HILTI Corporation was employed, whose curing temperature ranges from −5 °C to 40 °C, and setting and curing time are 30 min and 12 h at a substrate temperature of 20 °C, respectively. The mix proportion of the MOC adhesive mortar is presented in Table 3.

Table 3. The mix proportion of magnesium oxychloride cement.

Composition	MgO	$MgCl_2$	H_2O	Water Cement Ratio
Mass ratio	1000	384	276.8	0.2

2.3. Strengthening and Fire-Protection

2.3.1. BSP Strengthening

The BSP strengthening technique was applied to five RC beams after 28-days curing under laboratory conditions, as shown in Figure 2:

1. Bolt holes with a diameter of 14 mm were drilled in the steel plates.
2. Bolt holes with a diameter of 14 mm and a depth of 92 mm were drilled in to the side faces of the RC beams.
3. Washers were attached onto the concrete surface around the holes by silicone glass adhesive to prevent the adhesive mortar from leaking.
4. Adhesive mortar was injected into the holes and anchor bolts were inserted.
5. The steel plates were fixed on the RC beam side faces by using hex nuts after 24-h curing of adhesive mortar.

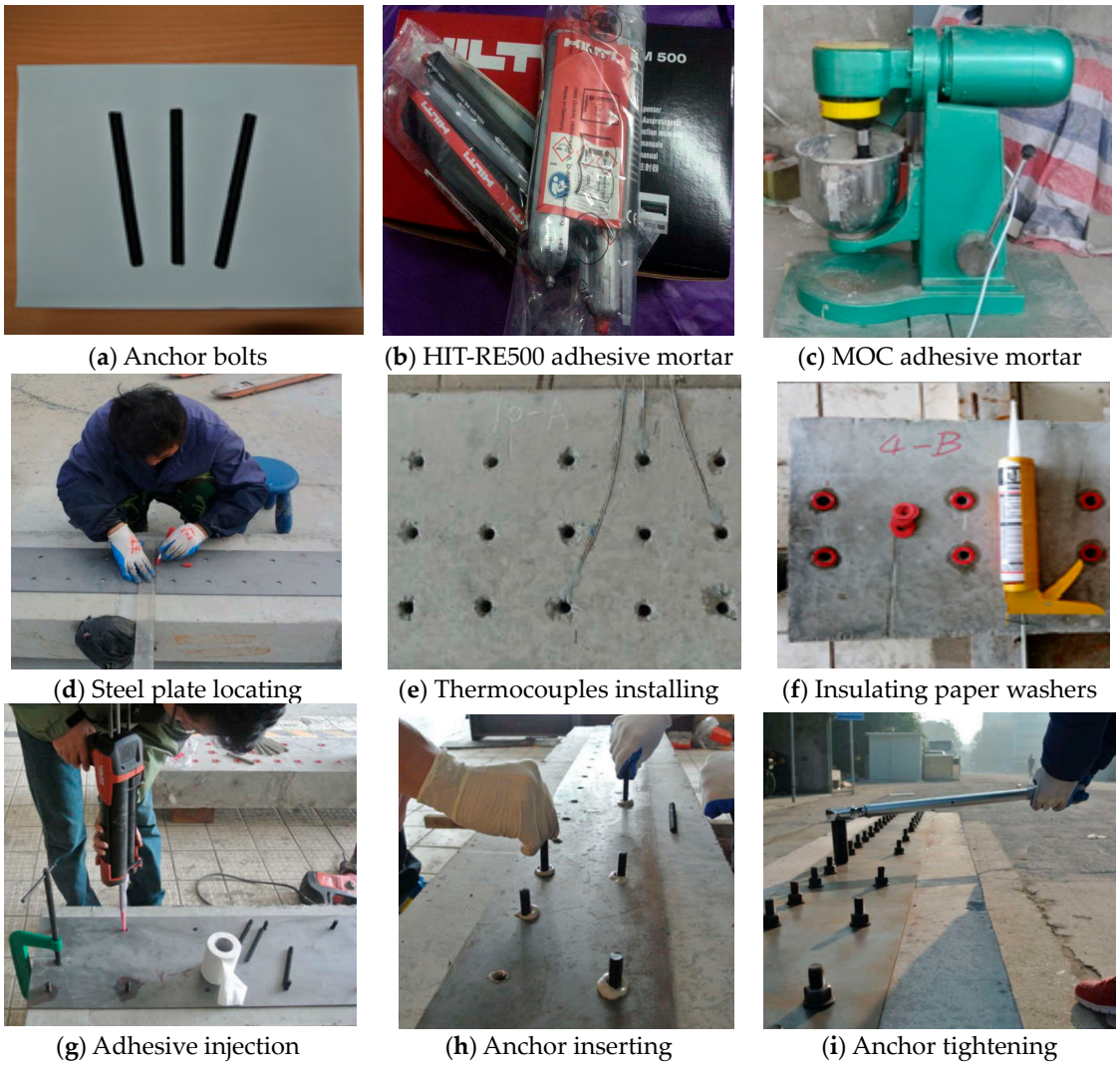

(**a**) Anchor bolts (**b**) HIT-RE500 adhesive mortar (**c**) MOC adhesive mortar

(**d**) Steel plate locating (**e**) Thermocouples installing (**f**) Insulating paper washers

(**g**) Adhesive injection (**h**) Anchor inserting (**i**) Anchor tightening

Figure 2. The strengthening procedure.

2.3.2. Fire Protection

The fire protection material used for P2B1-MOCT and P3B1-MOCT was the Interchar 1120 brand supplied by AkzoNobel Ltd. Co. (Amsterdam, Netherlands). The material should be applied at air and

substrate temperature between 10 °C and 40 °C, and a relative humidity less than 80%. The fireproof coating could intumesce at elevated temperature, thus providing an insulating layer on the specimen surface and preventing it from being heated up too rapidly. The construction steps were as follows:

1. The surface of anchor bolts and steel plates were cleaned and prepared;
2. The epoxy primers were brushed on the steel surface;
3. The fireproof coating was brushed over the primers evenly three times a day up to 3 mm thickness.

2.4. Test Procedure

2.4.1. Fire Test

A furnace of 4.5 m × 3.0 m × 1.7 m in the Structure Engineering and Fire Resistance Laboratory at Tongji University was used to conduct the fire test. The temperature elevation follows the ISO 834 temperature curve. The specimens P2B1-MOCT and P3B1-MOCT were heated on both the tensile soffit and two side faces. A spreader beam was used to impose two concentrated loads (i.e., 50% of the designed bearing capacity) on the RC beams to simulate the service load, which were kept constant throughout the heating process. Two hours of heating time was chosen herein according to the fire resistance time of the fire protection material and the requirements of the Code for Fire Protection Design of Building in mainland China. After fire exposure, the specimens were unloaded and cooled down naturally for 24 h. A general view of the fire test is shown in Figure 3.

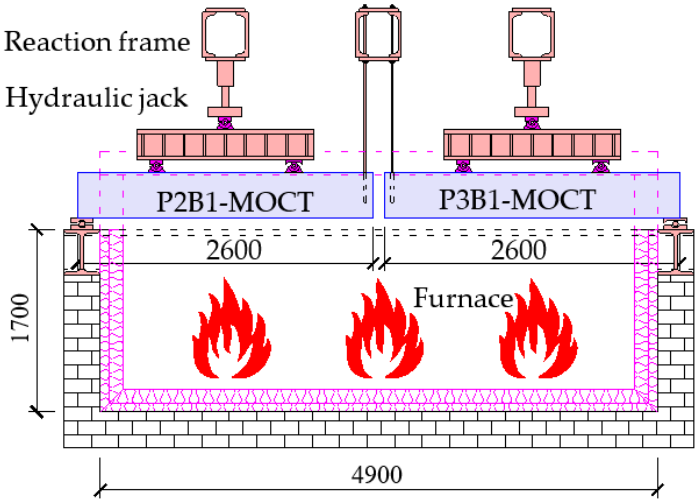

Figure 3. General view of the fire test (dimensions in mm).

To obtain the temperature distribution of concrete and anchor adhesive under fire, fourteen NK-162S thermocouples were installed in the RC beams to calibrate the temperature development. The temperature field and the strains as well as the displacements were collected by the data acquisition system produced by Jiangsu Donghua Testing Technology Co., Ltd., which is located in the Jingjiang City, China. The arrangement of thermocouples in P2B1-MOCT and P3B1-MOCT was shown in Figure 4a, where "M" represents the mid-span and the following number represents the distances between the thermocouple and the beam bottom surface in decimetre. Nine thermocouples were embedded in the bolt holes to investigate the temperature of the bolt anchoring system, as shown in Figure 4b, where "M", "L" and "R" represent the mid-span, the left and right shear span, and the subsequent number represents the distances of the thermocouple from the beam bottom surface in decimetre. The number after "D" represents the embedment depths of the thermocouples in mm.

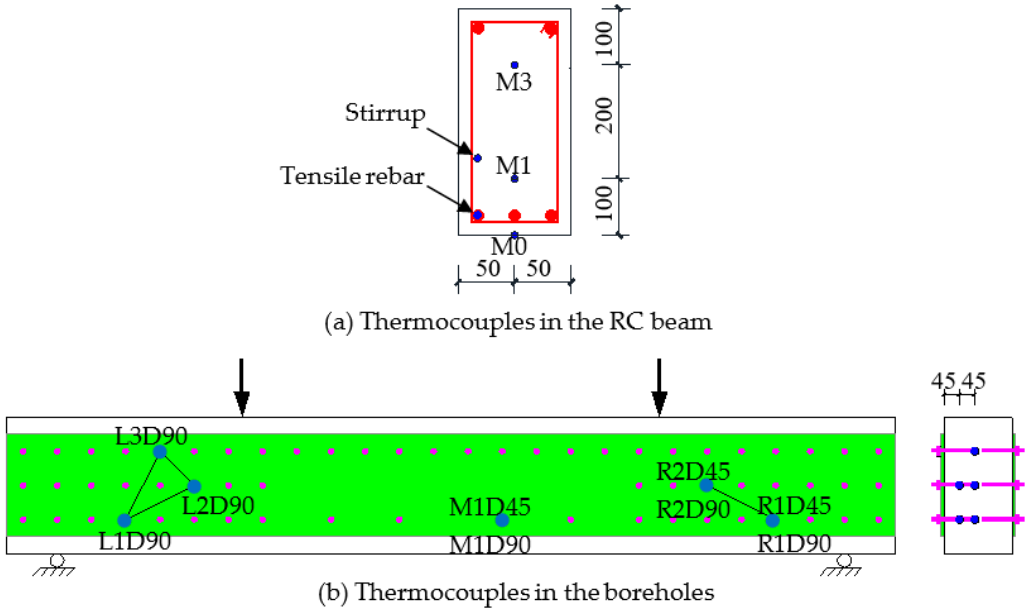

Figure 4. Arrangements of thermocouples for specimens under fire.

2.4.2. Four-Point-Bending Shear Test

This four-point-bending shear tests were also conducted in the Structure Engineering and Fire Resistance Laboratory at Tongji University. The clear span between the two supports was 2300 mm. A reaction frame equipped with a 2000 kN hydraulic jack was used to conduct the monotonous static loading. The load provided by the hydraulic jack was equally divided into two concentrated loads by a spreader beam, as shown in Figure 5. The shear span between the support and the nearest loading point was 540 mm; the shear-span ratio was 1.5. A force-control and multi-stage loading scheme was adopted: the load increment was 10 kN in the first stage, and then decreased to 5 kN when the external loads approached 85% of the designed peak bearing ability.

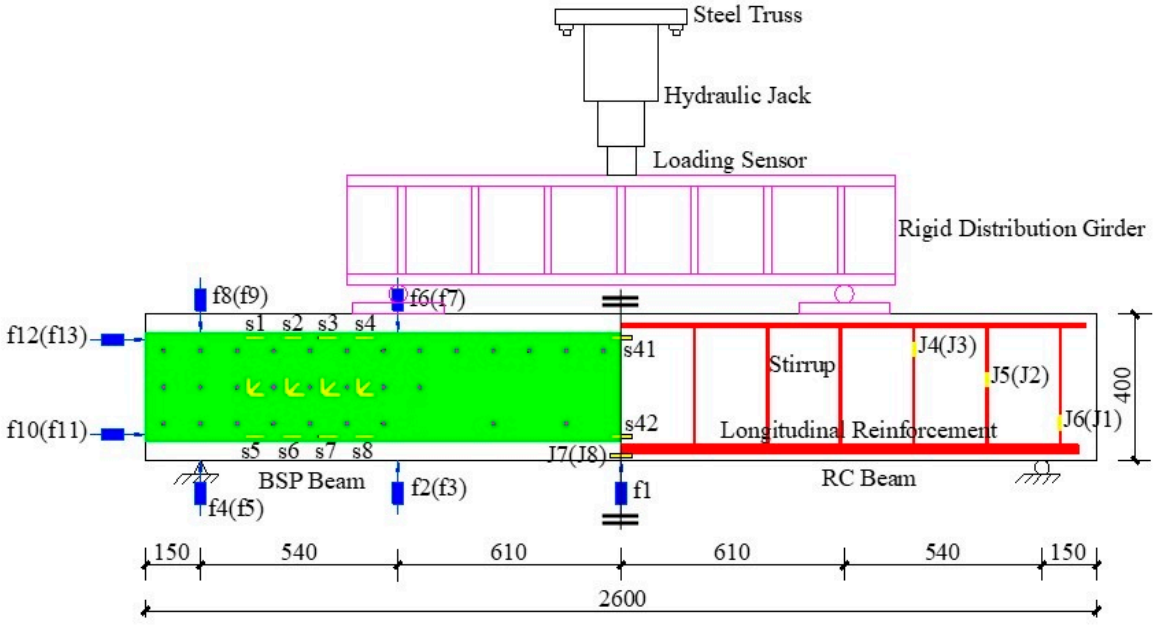

Figure 5. Set-up of the four-point-bending shear test and the layout of the strain gauges and LVDTs.

Five linear variable differential transducers (LVDTs) were employed to measure the displacements of supports, the mid-span and the loading points. Besides, four LVDTs were installed at the loading points and supports to obtain the transverse relative slips between the RC beam and the bolted steel plates. Another four LVDTs were used at both ends of the bolted steel plates to calibrate the longitudinal relative slips. The strains of longitudinal and transverse reinforcements, as well as the steel plates, were measured by BX120-3AA strain gauges, with a sensitivity coefficient of 2% ± 1%. The strain gauges were manufactured by Zhejiang Huangyan Testing Apparatus Factory, which is located in the Taizhou City, China.

3. Result Discussion

3.1. Thermal Response

The temperature development in specimen P3B1-MOCT is illustrated in Figure 6, and details about the highest temperature occurrence time are tabulated in Table 4. The temperature-time development curves of the furnace and the ISO834 heating curve are also both presented for comparison.

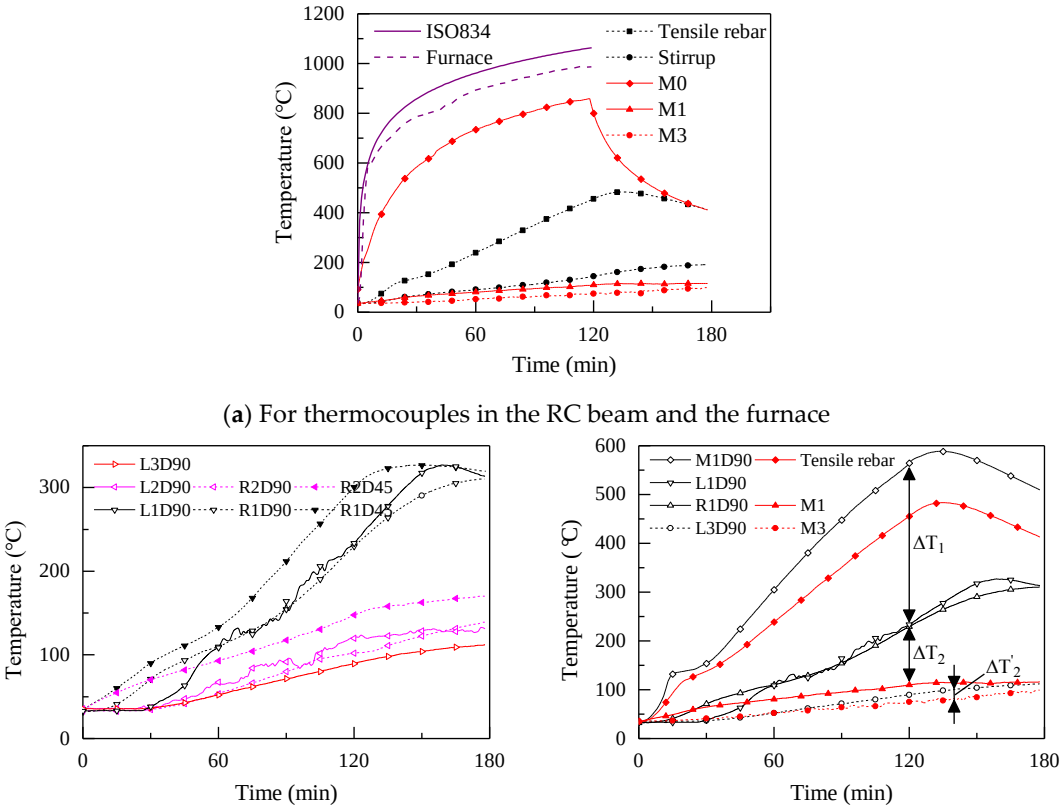

(**a**) For thermocouples in the RC beam and the furnace

(**b**) For thermocouples in the boreholes (1)

(**c**) For thermocouples in the boreholes (2)

Figure 6. The temperature development of P3B1-MOCT.

Table 4. The measure point serial number and highest temperature occurrence time of boreholes.

No.	T_{max} (°C)	Time (min)	No.	T_{max} (°C)	Time (min)
Furnace	989	120	M1D90	588	138
M0	859	120	R2D90	139	178
M1	116	180	R1D90	310	180
M3	100	178	R2D45	170	177
L3D90	112	180	R1D45	327	148
L2D90	133	176	Tensile rebar	483	136
L1D90	327	163	Stirrup	191	177

It is shown in Figure 6a that the average temperature was 35 °C before heating, and the temperatures of all measuring points increased with time. The temperature curve of the furnace was slightly lower than the ISO834 heating curve due to the unenclosed furnace. The highest temperature of the furnace was 989 °C, occurring at the flameout time, which was lower than that of the ISO834 heating curve (1065 °C). It was also evident that the temperature decreased as the increases of the distance from the measuring point to the beam bottom surface. The values and variation trend of the temperature on the beam bottom surface was rather similar to that of the furnace, with the maximum temperature of 859 °C appearing at the flameout moment. The highest temperatures of the measuring point d100 and d300 were 116 °C and 100 °C, occurring at 58 min after flameout. The maximum temperature of the tensile rebar and stirrup were recorded as 483 °C and 191 °C, appearing at 16 min and 57 min after flameout, respectively. The increasing temperature in interior concrete after flameout was mainly caused by the poor heat conductivity of concrete and the evaporation of the moisture, thus the heat continually transmitted from the exterior concrete to the interior even after shut off the fire.

It is evident from Figure 6b,c that the temperatures of different measuring point increase proportionally in the initial two hours. For the same borehole, the temperature at 45 mm embedment depth was higher than that at 90 mm embedment depth (for instance R1D45 > R1D90, R2D45 > R2D90). In addition, the temperatures of boreholes decreased with the increase of their distance from the beam bottom surface (for instance L1D90 > L2D90 > L3D90, R1D45 > R2D45). It is evident from Figure 6c that because the thermocouple at M1D90 contacted with the embedded end of the anchor bolt shaft, its temperature was close to the temperature on the concrete surface and even greater than that of the tensile rebar, due to the large heat conductivity of the bolt shaft. However, since the thermocouples at L1D90 and R1D90 did not contact with the bolt shaft, the temperatures decreased considerably due to the poor heat conductivity of MOC and concrete (for instance L1D90 ≈ R1D90 ≪ M1D90, and the discrepancy was ΔT_1 = 330 °C). However, the temperatures at the bottom of holes were still much greater than other positions in concrete (for instance R1D90 ≫ M1, L3D90 ≫ M3, and the discrepancies were ΔT_2 = 120 °C and $\Delta T_{2'}$=20 °C respectively), which indicated the post-installed anchor bolts would affect the temperature field of the specimens significantly. This phenomenon was mainly caused by the high heat conductivity of the bolt shaft, which resulted in higher temperature in the boreholes. Thus, if there are a large number of small-spaced anchors in the side faces of the BSP beam, the inner concrete temperature would be much higher than that of an unstrengthened concrete beam, which might affect the bearing capacity of the post-fire BSP beam to a lager extent.

As the temperature increased during fire exposure, the fire protective coatings on the surface of the steel plates began to expand and changed into char. The concrete colour after fire turned pale-yellow, and a large number of small visible cracks appeared on the beam surface. The spalling of concrete cover from beam bottom surface caused the exposure of steel bars. The comparisons of the fire protective coatings before and after fire exposure are shown in Figure 7.

(**a**) Primers brushing

(**b**) Intermediate coats brushing

Figure 7. *Cont*.

(**c**) Beam surface after fire

Figure 7. Construction of fire protective coating and post-fire phenomenon.

3.2. *Failure Modes and Crack Patterns*

3.2.1. Failure Mode

The failure modes of all specimens are shown in Figure 8, where shear failure occurred in all the specimens except P3B1-MOCT. Three representative failure modes could be found: the shear-tension (ST) failure, the shear-compression (SC) failure and the mid-span flexural (MF) failure.

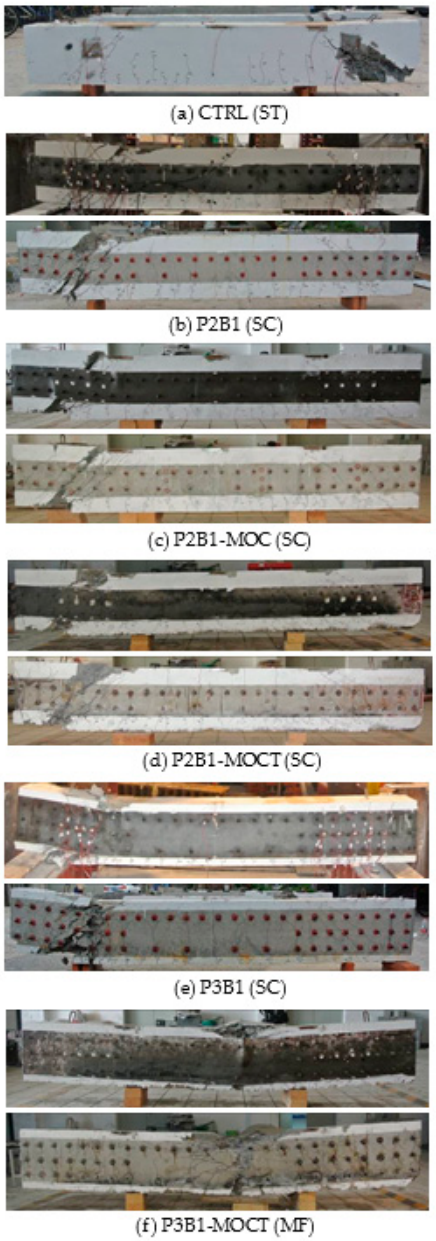

Figure 8. Failure modes of all BSP specimens.

The shear-tensile failure mode appeared in specimen CTRL. The specimen failed suddenly after the main diagonal crack emerged, as shown in Figure 8a, which was mainly caused by the yielding of stirrups due to the low stirrup ratio. The shear-compression failure was found in the specimens P2B1, P2B1-MOC, P2B1-MOCT, and P3B1, as shown in Figure 8b–e. This failure mode was caused by the combination of shear stress and compressive stress, which leads to concrete crushing and several diagonal cracks in the shear span. Diagonal cracks propagated from the hinged support to the loading point, the widths and the number of cracks increased with the increase of load, and the later emerged diagonal cracks were paralleled to the critical one. The mid-span flexural failure mode only occurred in specimen P3B1-MOCT due to the concrete crushing and the development of the vertical cracks in the pure bending zone, as shown in Figure 8f, which showed a satisfactory ductility.

3.2.2. Crack Patterns

The crack patterns of all specimens are shown in Figure 8. During the test, the cracks as well as their width were observed by using HC-CK101 crack width measuring instrument, which can achieve multiple magnifications with a probe. For CTRL, several vertical cracks firstly appeared near the mid-span, then the first visible diagonal crack initiated in the shear span, and more flexural and inclined cracks emerged as the load increased. A stirrup in the right shear span ruptured suddenly and the concrete fractured along the main diagonal crack at the same time without any warning. For P2B1-MOC, the vertical cracks first appeared and then the shear cracks occurred. Afterwards, the RC beam was divided into two parts and destroyed suddenly due to the formation of the punching section, the right parts was pushed downward while the left shear span moved upward. For P2B1, P2B1-MOCT and P3B1, the crack propagation and the failure modes were approximately the same as those of P2B1-MOC. For P3B1-MOCT, the flexural cracks first appeared and then the diagonal cracks appeared. With the increase of the external load, concrete at the top of mid-span began to crush and the compressive rebar began to yield. The number of diagonal cracks in P3B1-MOCT was obviously less than that in the specimens that failed in shear.

The cracking loads of all the specimens are summarized in Table 5. The load of the first flexural crack ranged from 0.06 P_u to 0.14 P_u, which indicates that the flexural cracking load was independent of the strengthening methods, temperature environment and the type of anchor adhesive mortar. The loads when the first diagonal crack occurred in CTRL, P2B1 and P3B1 were 212 kN, 401 kN and 500 kN (ranged from 0.23 P_u to 0.35 P_u), indicating that the occurrence time of the first diagonal crack was delayed after retrofitting. Meanwhile, the diagonal cracking load in the BSP specimens increased with the depth of steel plates. By comparing the cracking loads of P2B1 (400 kN), P2B1-MOC (401 kN), P2B1-MOCT (500 kN) and P3B1-MOCT (503 kN), and it is found that the load of the first diagonal crack was irrelevant to the anchor adhesive mortar and high temperature.

Table 5. The cracking loads and the shear capacities of specimens.

Specimen	P_f (kN)	P_d (kN)	P_u (kN)	P_f/P_u	P_d/P_u	$P_u/P_{CTRL}-1$	Failure Mode
CTRL	126	212	942	0.13	0.23	–	ST
P2B1	160	400	1174	0.14	0.34	25%	SC
P3B1	85	500	1409	0.06	0.35	50%	SC
P2B1-MOC	125	401	1230	0.1	0.33	31%	SC
P2B1-MOCT	263	315	1158	0.11	0.27	23%	SC
P3B1-MOCT	140	503	1292	0.11	0.39	37%	MF

Notes: P_f & P_d: the cracking loads when the first flexural or diagonal crack occurs; P_u: the ultimate load (shear capacity); P_{CTRL}: the ultimate load of the specimen CTRL; ST: shear-tension failure; SC: shear-compression failure; MF: mid-span flexural failure.

It is worth noting that both the majority of flexural and diagonal cracks passed through the anchor bolts, thus forming a bolt-centred radial pattern. This is because anchor bolts act as the medium to transfer the force from the RC beam to the steel plate, and thus a complicated stress

distribution formed in this region. The phenomenon of the buckling of the bolted steel plates is shown in Figure 9: the bulking of the steel plate for P2B1-MOCT occurred in the shear span, while that for P3B1-MOCT occurred in the mid-span. This indicates that buckling appeared at the place of the maximum compressive stress.

(**a**) in the left shear span of P2B1-MOCT

(**b**) in the mid-span of P3B1-MOCT

Figure 9. Buckling of the bolted steel plates.

3.3. Strength, Stiffness and Ductility

3.3.1. Shear Capacity

The load-deflection curves and the ultimate loads of all specimens are shown in Figure 10 and Table 5. The curves show that the beams exhibited two stages in the loading process: the linear growth stage and the slope decreasing stage. In the first stage, the curves presented linear growth when the external loads were approximately smaller than 80% of the peak loads, the initiation and growth of flexural cracks were mainly in this stage. In the second stage, the slope of the curves decreased significantly due to the yielding of longitudinal and transverse reinforcements. It is also visible that the BSP beams had the greater load bearing capacity and deformability than the CTRL beam.

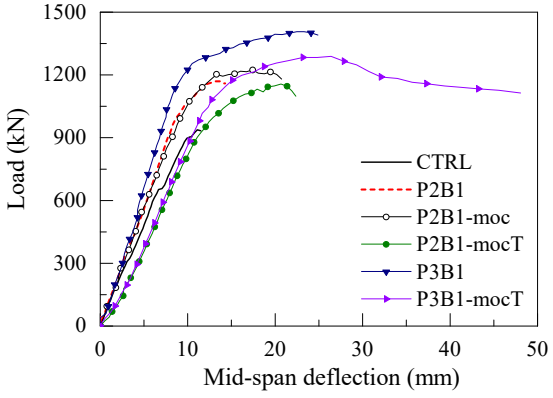

Figure 10. Load−mid-span deflection curves of tested specimens.

To compare the influence of various factors on the shear capacity, the six specimens were divided into three groups, i.e., group A (CTRL, P2B1, P3B1), group B (P2B1, P2B1-MOC) and group C (P2B1-MOC, P2B1-MOCT, P3B1-MOCT). Through the data analysis of the group A, it is found that the shear capacities were improved by 25% in P2B1 and 50% in P3B1 when compared with CTRL, respectively. The results proved that with the same bolt spacing, the shear capacity of the BSP beam with steel plates of 300 mm in depth is 25% higher than that with steel plates of 200 mm in depth. For group B, the difference of the shear capacity was 6% (i.e., 25–31%) in comparison to CTRL, which showed that the enhancement due to MOC is slightly better than that due to HIT-RE500. The analysis results of group C indicated that the high temperature was an unfavourable factor to the shear capacity of BSP beams. With the same steel plate depth and anchor adhesive mortar, P2B1-MOCT exhibited a relative decrease of 8% (i.e., 23–31%) in the shear capacity, as compared to P2B1-MOC. However, although the BSP beams were exposed to fire, their residual shear capacities were still greater than that of CTRL. For example, the shear capacities of P2B1-MOCT and P3B1-MOCT are 23% and 37% greater than that of CTRL. In general, the residual shear capacities of BSP beams after fire are satisfactory by using MOC as anchor adhesive mortar, and it could be effectively improved by increasing the plate depth.

3.3.2. Stiffness

An equivalent elasto-plastic theory was introduced according to the shape of the load–deflection curves to quantitatively analyse the stiffness and ductility of the specimens, as shown in Figure 11. The stiffness of specimens was characterized by the secant modulus K_e at the point on the ascending branch where $P = 0.75\,P_u$. This is because most specimens (except specimen P3B1-MOCT) exhibited brittle shear failure and no descending branches in the load-deflection curve. Therefore, the point where $P = P_u$ was defined as the end point D_{max}, which represents the maximum mid-span deflection.

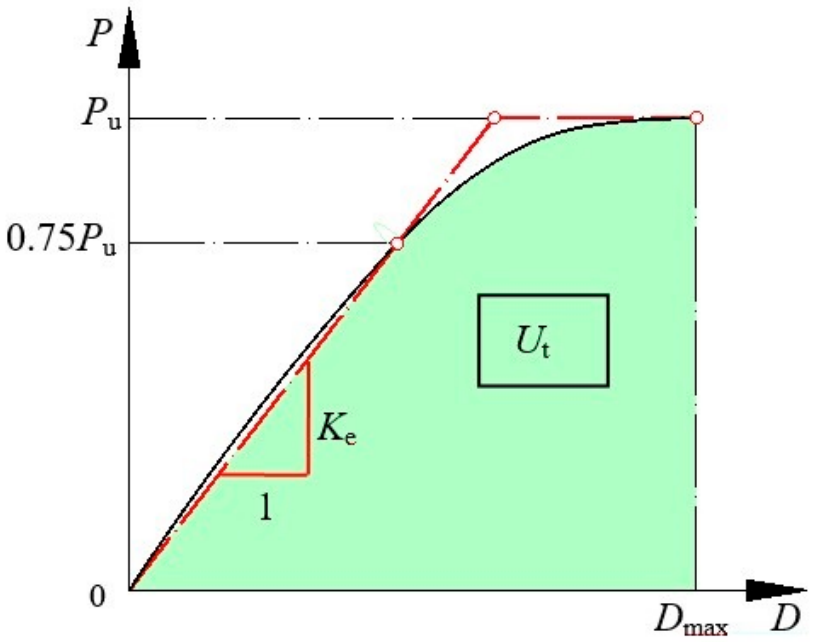

Figure 11. Equivalent elasto-plastic system of the load-deflection curve.

Figure 10 shows that the BSP beams exhibited a greater stiffness compared to CTRL, while the BSP beams subjected to fire presented a lower stiffness. This illustrates that the BSP strengthening technique played a positive role in the promotion of stiffness. In the earlier loading stage, the stiffness remained unchanged because the longitudinal rebars and stirrup were elastic. There was a dramatic dropping in stiffness when the stirrup began yielding or the concrete began crushing.

The stiffness of all the specimens are tabulated in Table 6. This shows that the stiffness was improved by 27% in P2B1 and 46% in P3B1 compared to CTRL, respectively. This indicates that at the same bolt spacing of 100 mm, the stiffness of P3B1 with a plate depth of 300 mm was 19% higher than that of P2B1 with a plate depth of 200 mm. As for the influence of anchor adhesive mortar, a comparison between P2B1 and P2B1-MOC indicates that the stiffness improvement of P2B1 with HIT-RE500 was 8% (i.e., 19–27%) greater than that of P2B1-MOC with MOC. It clearly shows that fire could reduce the stiffness of BSP specimens, even lower than that of CTRL. In summary, the increasing of plate depth could improve the stiffness significantly, while the fire would reduce the stiffness seriously. For the type of anchor adhesive mortar, the enhancement in stiffness for the BSP beams with HIT-RE500 is slightly better than that of those with the MOC.

Table 6. The stiffness, maximum deflection and ductility of specimens obtained from tests.

Specimen	Stiffness		Maximum Deflection		Modulus of Toughness	
	K_e (kN/mm)	Improvement	D_{max} (mm)	Improvement	U_t (kN.mm)	Improvement
CTRL	92.0	–	11.5	–	6019.4	–
P2B1	116.5	27%	14.3	24%	10,894.7	81%
P3B1	133.9	46%	25.0	117%	27,752.6	362%
P2B1-MOC	109.3	19%	20.2	76%	17,974.4	199%
P2B1-MOCT	81.5	−11%	21.9	90%	17,103.7	184%
P3B1-MOCT	86.4	−6%	28.5	147%	27,101.9	350%

3.3.3. Ductility

The modulus of toughness (U_t) was employed to quantify the ductility, i.e., the area under the load–deflection curve, which represents the amount of energy the specimen absorbed in the whole loading process, as shown in Figure 11.

The maximum deflections D_{max} and the modulus of toughness U_t are presented in Table 6. Though the BSP specimens had been exposed to fire, the D_{max} and U_t values were still higher than that of CTRL. P3B1-MOCT had the highest D_{max} and U_t, while P2B1 showed the least among all the BSP beams. The D_{max} and U_t were improved by 24% and 81% in P2B1, and 117% and 362% in P3B1 compared to CTRL, respectively. In other words, the improvement of D_{max} and U_t for P3B1 was 93% and 281% higher than that in P2B1 with the same bolt spacing of 100 mm. In addition, a comparison was made between P2B1 and P2B1-MOC, and the results indicate that the improvement of D_{max} and U_t for P2B1 were 52% and 118% higher than those for P2B1-MOC. This demonstrates that the anchor adhesive of MOC was more effective than HIT-RE500 for improving the ductility. Furthermore, the improvement of D_{max} for P3B1-MOCT was 57% higher than that for P2B1-MOCT due to the increase in plate depth from 200 mm to 300 mm. The failure mode, which transferred from the shear-compression failure in P2B1-MOCT to the mid-span flexural failure in P3B1-MOCT due to the increase of steel plate depth, indicates that the post-fire ductility of BSP beams has been effectively improved by increasing the depth of the bolted steel plates. The anchor adhesive of MOC can retain the original ductility and deformability of BSP beams, since the comparison between P2B1-MOC and P2B1-MOCT shows no clear difference in D_{max} and U_t.

3.4. Strain Development

3.4.1. Strains of Stirrups

The layout of strain gauges in stirrups and tensile reinforcements is shown in Figure 5. Considering the strain development of stirrups in shear span was similar for all specimens, Figure 12 only shows the strain development of specimen P2B1-MOC. From the comparison among the strain gauges j1, j2, j4, j5 and j6 (j3 damaged before the test), strains increased with the external load, while j2 and j5 tended to reach a higher value in a certain load after 800 kN. In addition, only j2 yielded, with a strain of 2346 με, which corresponds to the shear-compression failure mode in the left shear span.

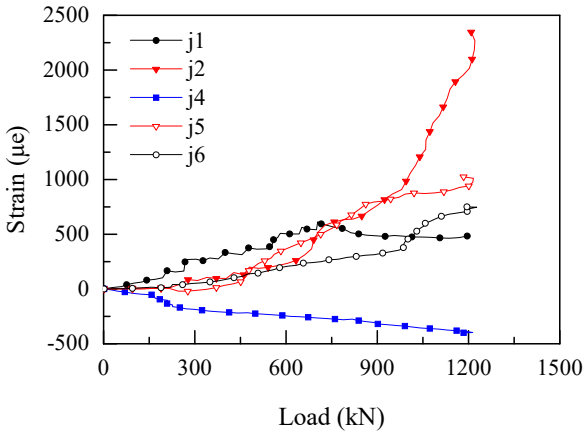

Figure 12. The strains of stirrups in the shear span of P2B1-MOC.

For P2B1-MOCT and P3B1-MOCT, the initial stress had risen in the steel plates and anchor bolts; it was impossible to stick strain gauges on the stirrups in the concrete without removing the steel plates and anchor bolts. Therefore, no strain gauges were attached to stirrups. The curves of the external load and the corresponding maximum strains of stirrups are shown in Figure 13. Three typical linear stages were observed in the whole loading process except CTRL, which only has two. In the first stage, the slopes were rather small and were almost parallel to the *X* axis, since the shear resistance in the initial loading stage was mainly supplied by the concrete. The first turning point of the curves appeared with the first diagonal crack, and afterwards the slopes increased drastically in the second stage. In the third stage, the slopes of the curves (except CTRL) changed sharply after the strain values of the stirrup reached to 2000 με, which indicated the yielding of the stirrup in the shear span. Moreover, in the second stage, the strain of the stirrups in the BSP specimens were lower than that in CTRL under the same external load. This phenomenon proved that the load originally resisted by the stirrups had transferred to the bolted steel plates partially; hence, the BSP technique could relieve the tensile stress of stirrups. In addition, the strain of P2B1 was higher than that of P2B1-MOCT at a certain load, which indicates that the anchor adhesive of MOC was more effective than HIT-RE500 in stress transfer.

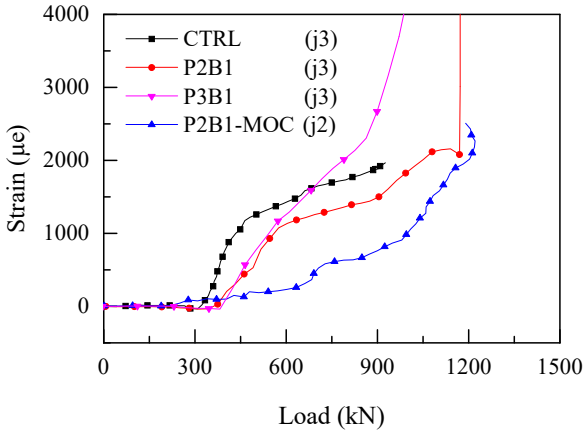

Figure 13. The maximum strains of stirrups of the unfired specimens.

3.4.2. Strains of Tensile Reinforcement

New strain gauges were attached to the tensile reinforcement in the pure bending zone for the post-fire BSP beams, and the post-added strain gauges were labelled as j7 and j8, as shown in Figure 5.

Figure 14 shows the mean value of strains of tensile longitudinal reinforcements in the mid-span for all specimens. It can be seen that there were two linear stages in each curve except P3B1. In the first

stage, the strains increased linearly, and turning points of the curves appeared when the strains reached 2000 με approximately. Furthermore, the ascending order of the strains in the tensile reinforcement under the same load was P3B1 ≪ P2B1-MOC < P2B1 < P3B1-MOCT < CTRL < P2B1-MOCT. Thus, the following conclusions can be drawn:

1. The deeper steel plates resulted in the smaller strains.
2. The specimens after fire intended to exhibit a greater strain, which indicates that the high temperature imposed a harmful influence on the BSP strengthening technique.
3. The difference in the strains of the tensile reinforcement caused by the anchor adhesive mortar was negligible.
4. The strains developed in the longitudinal rebar of P3B1-MOCT were larger than those of P2B1-MOCT when the external load reached the ultimate bearing capacity. This indicates that the tensile reinforcement sustains higher stress when the failure mode changed from shear-compression to mid-span flexural failure, i.e., the BSP technique is effective in the enhancement of not only the shear capacity but also the bending capacity.

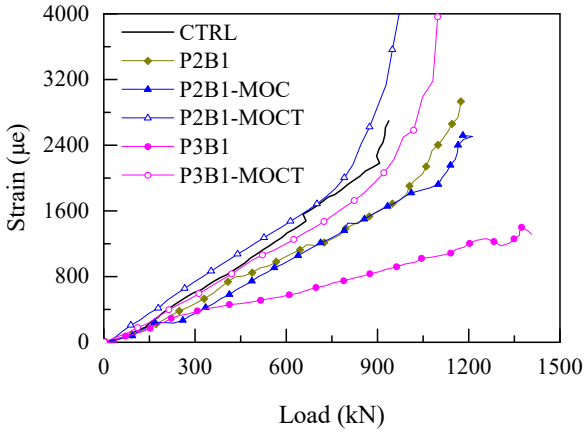

Figure 14. The mean strains of tensile longitudinal reinforcement in mid-span of all specimens.

3.4.3. Tensile and Compressive Strains of Steel Plates

To analyse the flexural behaviour of the steel plates, a total of sixteen strain gauges were attached to the upper and lower edges of the steel plates in the shear span, and another two strain gauges were employed in the mid-span. In addition, eight strain rosettes were attached along the centroidal level of the steel plates in the shear span to measure the principal strains. The arrangement of strain gauges and strain rosettes for the steel plates in the specimen P2B1-MOCT was shown in Figure 5. Then the principal strains, the shear strains and inclinations of the principal strains were calculated, and the maximum value of the strains under each level of loading were taken.

Due to the analogous strain distribution in the steel plates of all the BSP specimens, only strains in P2B1-MOCT and P3B1-MOCT were illustrated. The tensile and compressive strains developed in the steel plates in both the shear span and mid-span of P2B1-MOCT were shown in Figure 15a, and those of P3B1-MOCT were illustrated in Figure 15b. It is evident that the strains at the upper edge of the steel plate were negative and those at the lower edge were positive. Along the beam axis, the magnitudes of the strain gauges increased gradually from the support to the mid-span (for instance, |s1| < |s2| < |s3| < |s4|, |s5| < |s6| < |s7| < |s8|). The absolute strains at the lower edge of steel plate were found to be slightly higher than those at the upper edge (for example, |s5| > |s1|, |s6| > |s2|, |s7| > |s3|, |s8| > |s4|). This is because the compressive stress at the top of the beam was mainly resisted by concrete, while the lower tensile stress was resisted by both tensile rebars and steel plates; that is to say, the neutral axis was closer to the beam upper surface.

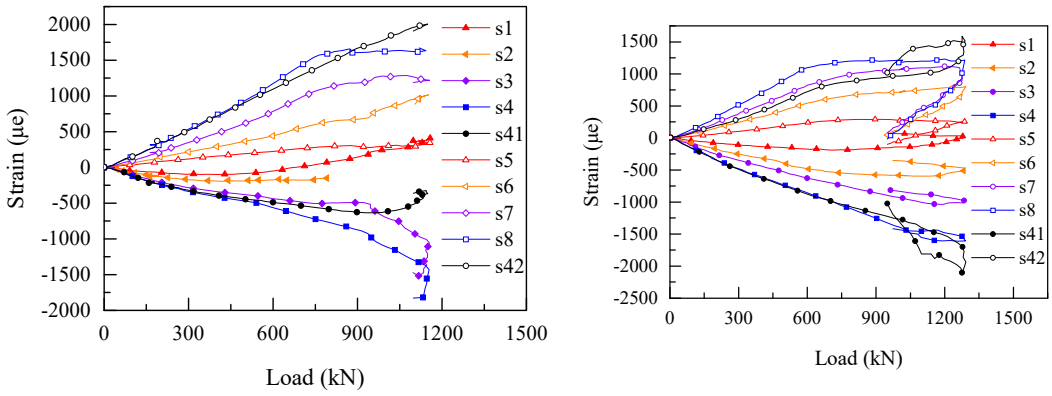

(**a**) P2B1-MOCT (**b**) P3B1-MOCT

Figure 15. The tensile and compressive strains of the steel plate in P2B1-MOCT and P3B1-MOCT.

On the other hand, at the early loading stage, the compressive and tensile strains developed in the steel plates of P3B1-MOCT followed the aforementioned trend as P2B1-MOCT, as shown in Figure 15b. However, the failure mode transfer from shear-compression to mid-span flexural failure, the crushing of concrete occurred, and the compressive stress shifted to the upper edge of the bolted steel plates. That is why the compressive strains in the steel plates increased drastically and became greater than the tensile strains (|s1| > |s5|, |s2| > |s6|, |s3| > |s7|, |s4| > |s8|).

3.4.4. Principal Strains of Steel Plates

The principal strains of the steel plate in the left shear span of P2B1-MOCT and P3B1-MOCT are shown in Figure 16. Along the longitudinal direction, the magnitudes of the principal strains are similar, indicating the shear stress along the shear span was uniform. The absolute magnitudes of the principal tensile and compressive strains were roughly equal in P2B1-MOCT ($|r_1, \varepsilon_{max}| \approx |r_1, \varepsilon_{min}|$, $|r_2, \varepsilon_{max}| \approx |r_2, \varepsilon_{min}|$). When shear-compression failure occurred, the distribution of the principal strain of the steel plate in the shear span was uniform. Unlike P2B1-MOCT, the absolute values of the principal tensile strain were higher than the principal compressive strain in P3B1-MOCT ($|r_1, \varepsilon_{max}| > |r_1, \varepsilon_{min}|$, $|r_2, \varepsilon_{max}| > |r_2, \varepsilon_{min}|$), which indicated that the steel plate in the shear span sustains more tensile force when the failure mode changed from shear-compression to mid-span flexural.

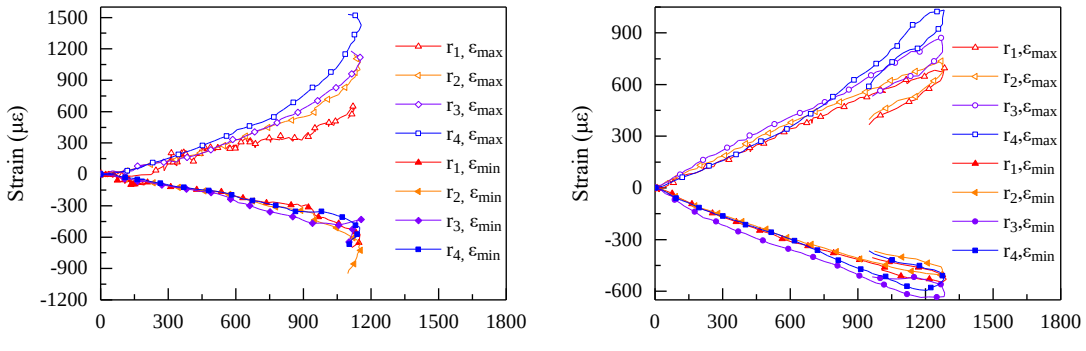

(**a**) P2B1-MOCT (**b**) P3B1-MOCT

Figure 16. The principal strains of the steel plate in the left shear span.

The shear strains and the inclinations of the principal strains in the shear span of P2B1-MOCT and P3B1-MOCT are shown in Figure 17. Similarly, the magnitudes of the shear strains were similar along the longitudinal direction. At the early loading stage, the inclinations of the tensile principal strains were close to 90°, but declined as the external load and the distance from the support increased

($|r_1, \alpha| > |r_2, \alpha| > |r_3, \alpha| > |r_4, \alpha|$). The ratio of bending action to shear action increased as the external load and the distance from the support increased.

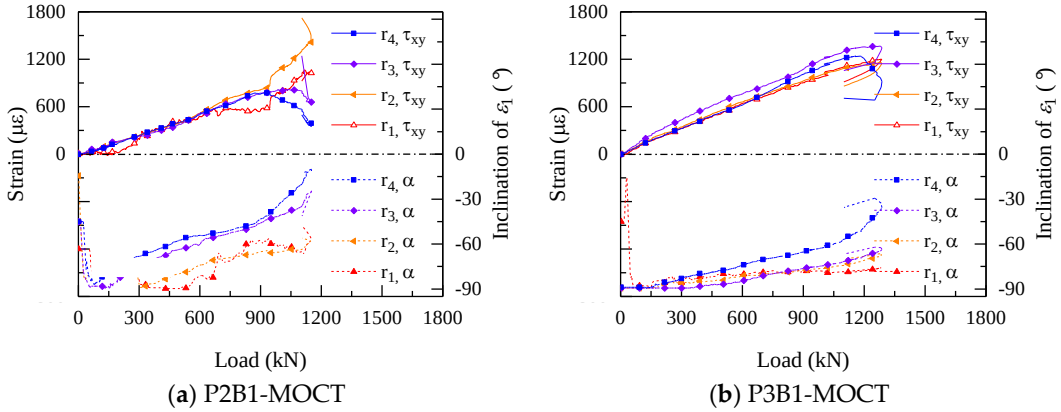

(**a**) P2B1-MOCT (**b**) P3B1-MOCT

Figure 17. The shear strains and inclinations of the principal strains of the steel plate.

3.5. Longitudinal and Transverse Slips

The BSP specimens strengthened by two bolted steel plates on both the side faces of the RC beams are composite members. Although the RC beam and the steel plates can co-work well, relative slips were still observed due to the shear deformability of the anchor bolts. The relative slips exert a direct influence on the collaboration between the RC beam and the steel plates, thus it is important to investigate the development of the transverse and longitudinal slips in the loading process. The arrangement of the LVDTs is shown in Figure 5. Considering the similar development of the relative slips, only the slips in P3B1-MOCT are illustrated in Figure 18.

As can be seen from Figure 18a, the magnitudes of the transverse slips at the loading points were positive and greater than those of negative ones above the supports, which indicates that there were uncoordinated deformations existing between the bolted steel plate and the RC beam. The longitudinal slips between the RC beam and the steel plates are shown in Figure 18b; it is obvious that the values of the longitudinal slips were rather small except at the f_{11} measure point. The relative longitudinal slips at the lower side of the steel plate were negative while those at the upper side were positive, because the steel plate in the shear span revolved with the direction of bending moment, but its revolution was less than that of the RC beam. Although the relative slips were rather small, which ranged from −3 mm to 3 mm for all BSP specimens, the transverse and longitudinal relative slips were crucial to the shear performance of BSP beams due to the great elastic modulus of steel. A small deformation could cause a considerable stress reduction in the bolted steel plate, leading to a serious decreased strengthening effect.

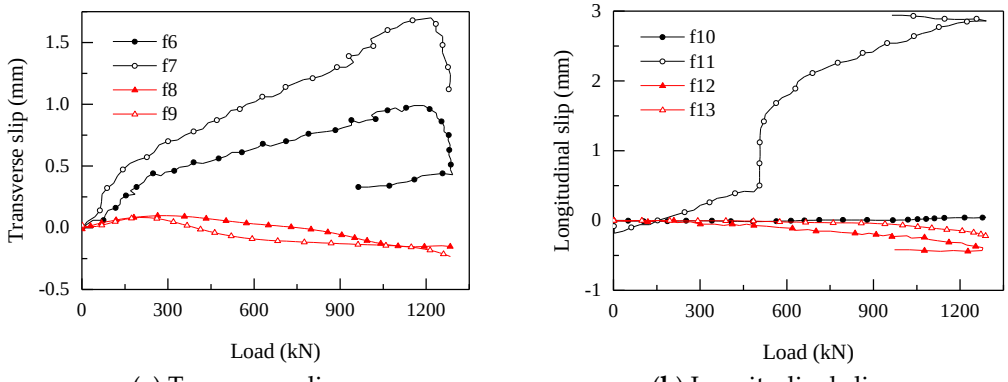

(**a**) Transverse slips (**b**) Longitudinal slips

Figure 18. Relative slips between the bolted steel plate and RC beam of P3B1-MOCT.

4. Conclusions

The shear performance of BSP beams and their post-fire performance have been investigated based on four-point-bending shear tests after exposure to fires. The main findings are summarized as follows:

During the fire test, the temperature of concrete decreased with the distance from the beam bottom and side surfaces, as well as the embedment depth in the same hole. Three representative failure modes were observed in the post-fire test: the brittle shear-tension failure for specimen CTRL, the mid-span flexural failure for P3B1-MOCT, and the shear-compression failure for the rest specimens.

The load of the first flexural crack ranged from 0.06 P_u to 0.14 P_u for all the specimens, which indicates that the flexural crack load was independent of the depth of the bolted steel plate, the temperature, and the category of anchor adhesive mortar. The first diagonal crack in the BSP specimens appeared later than that in CTRL, which was controlled by the plate depth and bolt spacing, but irrelevant to the type of anchor adhesive and temperature environment.

The shear capacity, stiffness and ductility of the BSP beams were greater than CTRL. The anchor adhesive of MOC is more efficient than HIT-RE500 for enhancing the shear capacity and ductility, and a smaller improvement in stiffness. Moreover, although the stiffness of the post-fire BSP beams is lower than that of CTRL, BSP beams exhibit a higher ductility and shear capacities. Thus, increasing the depth of the steel plates could effectively improve the residual shear capacity of BSP beams after exposing to fire.

The tensile and compressive strains of the bolted steel plates increased gradually along the beam axis from the support to the mid-span, and the strains at the lower edge were higher than that at the upper edge. In addition, the longitudinal reinforcement strains of the post-fire BSP beams were greater than that in the unfired BSP beams. Thus, the failure modes changed from shear failure to mid-span flexural failure.

The longitudinal and transverse relative slips proved the uncoordinated deformation between the bolted steel plates and the RC beam, as well as the lagged deformation of the steel plates.

Author Contributions: Conceptualization, L.-Z.L.; Data curation, X.L., Y.C.; Funding acquisition, L.-Z.L., Z.-D.L.; Investigation, X.L.; Methodology, L.-Z.L., K.-Q.Y.; Supervision, L.-Z.L., Z.-D.L.; writing—original draft preparation, X.L.; Writing—review& editing, L.-Z.L., M.-N.S.

Funding: The research described here received financial support from the National Natural Science Foundation of China (Project No. 51778496 and No. 51778497), and Fundamental Research Funds for Central Universities of China.

Conflicts of Interest: The authors declare no conflict of interest.

References

1. Chen, M.T.; Young, B. Material properties and structural behavior of cold-formed steel elliptical hollow section stub columns. *Thin-Walled Struct.* **2019**, *134*, 111–126. [CrossRef]
2. Zhou, J.; Wang, L. Repair of fire-damaged reinforced concrete members with axial Load: A review. *Sustainability* **2019**, *11*, 963. [CrossRef]
3. Wang, L.; Su, R.K.L.; Cheng, B.; Li, L.Z.; Wan, L.; Shan, Z.W. Seismic behavior of preloaded rectangular RC columns strengthened with precambered steel plates under high axial load ratios. *Eng. Struct.* **2017**, *152*, 683–697. [CrossRef]
4. Yang, Y.; Feng, S.Q.; Xue, Y.C.; Yu, Y.L.; Wang, H.Y.; Chen, Y. Experimental study on shear behavior of fire-damaged reinforced concrete T-beams retrofitted with prestressed steel straps. *Constr. Build. Mater.* **2019**, *209*, 644–654. [CrossRef]
5. Lai, M.; Hanzic, L.; Ho, J. Fillers to improve passing ability of concrete. *Struct. Concr.* **2019**, *20*, 185–197. [CrossRef]
6. Li, L.Z.; Cai, Z.W.; Yu, K.Q.; Zhang, Y.X.; Ding, Y. Performance-based design of all-grade strain hardening cementitious composites with compressive strengths from 40 MPa to 120 MP. *Cem. Concr. Compos.* **2019**, *97*, 202–217. [CrossRef]

7. Yu, K.Q.; Li, L.Z.; Yu, J.T.; Wanga, Y.C.; Ye, J.H.; Xu, Q.F. Direct tensile properties of engineered cementitious composites: A review. *Constr. Build. Mater.* **2018**, *165*, 346–362. [CrossRef]
8. Yu, K.; Li, L.; Yu, J.; Xiao, J.; Ye, J.; Wang, Y. Feasibility of using ultra-high ductility cementitious composites for concrete structures without steel rebar. *Eng. Struct.* **2018**, *170*, 11–20. [CrossRef]
9. Yu, K.Q.; Wang, Y.C.; Yu, J.T.; Xu, S.L. A strain-hardening cementitious composites with the tensile capacity up to 8%. *Constr. Build. Mater.* **2017**, *137*, 410–419. [CrossRef]
10. Ding, Y.; Yu, J.T.; Yu, K.Q.; Xu, S.L. Basic mechanical properties of ultra-high ductility cementitious composites: From 40 MPa to 120 MPa. *Compos. Struct.* **2018**, *185*, 634–645. [CrossRef]
11. Yu, K.Q.; Yu, J.T.; Dai, J.G.; Lu, Z.D.; Surendra, P.S. Development of ultra-high performance engineered cementitious composites using polyethylene (PE) fibers. *Constr. Build. Mater.* **2018**, *158*, 217–227. [CrossRef]
12. Weinberg, K.; Khosravani, M.R. On the tensile resistance of UHPC at impact. *Eur. Phys. J. Spec. Top.* **2018**, *227*, 167–177. [CrossRef]
13. Khosravani, M.R.; Weinberg, K. A review on split Hopkinson bar experiments on the dynamic characterisation of concrete. *Constr. Build. Mater.* **2018**, *190*, 1264–1283. [CrossRef]
14. Keshtegar, B.; Bagheri, M.; Yaseen, Z.M. Shear strength of steelfiber-unconfined reinforced concrete beam simulation: Application of novel intelligent model. *Compos. Struct.* **2019**, *212*, 230–242. [CrossRef]
15. Khosravani, M.R.; Nasiri, S.; Anders, D.; Weinberg, K. Prediction of dynamic properties of ultra-high performance concrete by an artificial intelligence approach. *Adv. Eng. Softw.* **2019**, *127*, 51–58. [CrossRef]
16. Su, R.K.L.; Cheng, B.; Wang, L.; Siu, W.H.; Zhu, Y. Use of bolted steel plates for strengthening of reinforced concrete beams and columns. *IES J. Part A Civ. Struct. Eng.* **2011**, *4*, 55–68. [CrossRef]
17. Li, L.Z. New Partial Interaction Models for Bolted-Side-Plated Reinforced Concrete Beams. Ph.D. Thesis, The University of Hong Kong, Pokfulam Road, Hong Kong, China, 2013.
18. Li, L.Z.; Jiang, C.J.; Jia, L.J.; Lu, Z.D. Local buckling of bolted steel plates with different stiffener configuration. *Eng. Struct.* **2016**, *119*, 186–197. [CrossRef]
19. Liu, X.; Lu, Z.D.; Li, L.Z. The use of bolted side plates for shear strengthening of RC beams: A review. *Sustainability* **2018**, *10*, 4658. [CrossRef]
20. Park, D.G.; Cho, J.Y.; Oh, B.H. Failure behavior and separation criterion for strengthened concrete members with steel plates. *J. Struct. Eng.* **2003**, *129*, 1191–1198.
21. Yu, J.T.; Liu, K.K.; Li, L.Z.; Wang, Y.C.; Yu, K.Q.; Xu, Q.F. A simplified method to predict the fire resistance of RC Beams strengthened with near-surface mounted CFRP. *Compos. Struct.* **2018**, *193*, 1–7. [CrossRef]
22. Zhu, J.H.; Wei, L.L.; Moahmoud, H.; Redaelli, E.; Xing, F.; Bertolini, L. Investigation on CFRP as dual-functional material in chloride-contaminated solutions. *Constr. Build. Mater.* **2017**, *151*, 127–137. [CrossRef]
23. Zhu, J.H.; Su, M.N.; Huang, J.Y.; Ueda, T.; Xing, F. The ICCP-SS technique for retrofitting reinforced concrete compressive members subjected to corrosion. *Constr. Build. Mater.* **2018**, *167*, 669–679. [CrossRef]
24. Carpinteri, A.; Cornetti, P.; Lacidogna, G.; Paggi, M. Towards a unified approach for the analysis of failure modes in FRP-retrofitted concrete beams. *Adv. Struct. Eng.* **2009**, *12*, 715–729. [CrossRef]
25. Carpinteri, A.; Lacidogna, G.; Paggi, M. Acoustic emission monitoring and numerical modeling of FRP delamination in RC beams with non-rectangular cross-section. *Mater. Struct.* **2007**, *40*, 553–566. [CrossRef]
26. Oehlers, D.J.; Nguyen, N.T.; Ahmed, M.; Bradford, M.A. Transverse and longitudinal partial interaction in composite bolted side-plated reinforced-concrete beams. *Struct. Eng. Mech.* **1997**, *5*, 553–563. [CrossRef]
27. Nguyen, N.T.; Oehlers, D.J.; Bradford, M.A. An analytical model for reinforced concrete beams with bolted side plates accounting for longitudinal and transverse partial interaction. *Int. J. Solids Struct.* **2001**, *38*, 6985–6996. [CrossRef]
28. Su, R.K.L.; Zhu, Y. Experimental and numerical studies of external steel plate strengthened reinforced concrete coupling beams. *Eng. Struct.* **2005**, *27*, 1537–1550. [CrossRef]
29. Su, R.K.L.; Li, L.Z.; Lo, S.H. Longitudinal partial interaction in bolted side-plated reinforced concrete beams. *Adv. Struct. Eng.* **2014**, *17*, 921–936. [CrossRef]
30. Su, R.K.L.; Li, L.Z.; Lo, S.H. Shear transfer in bolted side-plated reinforced concrete beam. *Eng. Struct.* **2013**, *56*, 1372–1383. [CrossRef]
31. Siu, W.H.; Su, R.K.L. Effects of plastic hinges on partial interaction behaviour of bolted side-plated beams. *J. Constr. Steel Res.* **2010**, *66*, 622–633. [CrossRef]
32. Siu, W.H.; Su, R.K.L. Load–deformation prediction for eccentrically loaded bolt groups by a kinematic hardening approach. *J. Constr. Steel Res.* **2009**, *65*, 436–442. [CrossRef]

33. Su, R.K.L.; Siu, W.H. Nonlinear response of bolt groups under in-plane loading. *Eng. Struct.* **2007**, *29*, 626–634. [CrossRef]
34. Li, L.Z.; Lo, S.H.; Su, R.K.L. Experimental study of moderately reinforced concrete beams strengthened with bolted-side steel plates. *Adv. Struct. Eng.* **2013**, *16*, 499–516. [CrossRef]
35. Lo, S.H.; Li, L.Z.; Su, R.K.L. Optimization of partial interaction in bolted side-plated reinforced concrete beams. *Comput. Struct.* **2014**, *131*, 70–80. [CrossRef]
36. Li, L.Z.; Jiang, C.J.; Su, R.K.L.; Lo, S.H. Design of bolted side-plated reinforced-concrete beams with partial interaction. *Proc. Inst. Civ. Eng. Struct. Build.* **2016**, *169*, 81–95. [CrossRef]
37. Li, L.Z.; Jiang, C.J.; Su, R.K.L.; Lo, S.H. A piecewise linear transverse shear transfer model for bolted side-plated beams. *Struct. Eng. Mech.* **2017**, *62*, 443–453. [CrossRef]
38. Xu, X.L.; Lu, Z.D.; Li, L.Z.; Jiang, C.J. Numerical study on the local buckling behaviour of bolted steel plates in steel jacketing. *Adv. Mater. Sci. Eng.* **2017**, *2017*, 1352084. [CrossRef]
39. Li, L.Z.; Wu, Z.L.; Yu, J.T.; Wang, X.; Zhang, J.X.; Lu, Z.D. Numerical simulation of the shear capacity of bolted side-plated RC beams. *Eng. Struct.* **2018**, *171*, 373–384. [CrossRef]
40. Li, L.Z.; Liu, X.; Luo, Y.; Su, M.N.; Zhu, J.H. Flexural performance of bolted-side-plated reinforced concrete beams with local buckling restraining. *ACI Struct. J.* **2019**, *116*, 77–87.
41. Barnes, R.A.; Baglin, P.S.; Mays, G.C.; Subedi, N.K. External steel plate systems for the shear strengthening of reinforced concrete beams. *Eng. Struct.* **2001**, *23*, 1162–1176. [CrossRef]
42. Li, L.Z.; Cai, Z.W.; Lu, Z.D.; Zhang, X.L.; Wang, L. Shear performance of bolted side-plated reinforced concrete beams. *Eng. Struct.* **2017**, *144*, 73–87. [CrossRef]
43. Jiang, C.J.; Lu, Z.D.; Li, L.Z. Shear performance of fire-damaged reinforced concrete beams repaired by a bolted side-plating technique. *J. Struct. Eng. Asce* **2017**, *143*, 4017007. [CrossRef]
44. Department for Communities and Government. *Fire Statistics: Great Britain April 2013 to March 2014*; Department for Communities and Government: London, UK, 2015.
45. Jiang, C.J.; Yu, J.T.; Li, L.Z.; Wang, X.; Wang, L.; Liao, J.H. Experimental study on the residual shear capacity of fire-damaged RC frame beams and cantilevers. *Fire Saf. J.* **2018**, *100*, 140–156. [CrossRef]
46. Li, L.Z.; Liu, X.; Yu, J.T.; Lu, Z.D.; Su, M.N.; Liao, J.H.; Xia, M. Experimental study on seismic performance of post-fire reinforced concrete frames. *Eng. Struct.* **2019**, *179*, 161–173. [CrossRef]
47. Arioz, O. Effects of elevated temperatures on properties of concrete. *Fire Saf. J.* **2007**, *42*, 516–522. [CrossRef]
48. Kodur, V. Properties of concrete at elevated temperatures. *Isrn Civ. Eng.* **2014**, *2014*, 1–15. [CrossRef]
49. Kadhum, M.M. Fire resistance of reinforced concrete rigid beams. *J. Civ. Eng. Constr. Technol.* **2014**, *5*, 35–48.
50. Topcu, I.B.; Boga, A.R.; Demir, A. The effect of elevated temperatures on corroded and uncorroded reinforcement embedded in mortar. *Constr. Build. Mater.* **2010**, *24*, 2101–2107. [CrossRef]
51. Topcu, I.B.; Isikdag, B. The effect of cover thickness on rebars exposed to elevated temperatures. *Constr. Build. Mater.* **2008**, *22*, 2053–2058. [CrossRef]
52. Topcu, I.B.; Karakurt, C. Properties of reinforced concrete steel rebars exposed to high temperatures. *Res. Lett. Mater. Sci.* **2008**, *2008*, 1–4. [CrossRef]
53. Unluoglu, E.; Topcu, I.B.; Yalaman, B. Concrete cover effect on reinforced concrete bars exposed to high temperatures. *Constr. Build. Mater.* **2007**, *21*, 1155–1160. [CrossRef]
54. Ergun, A.; Kurklu, G.; Baspinar, M. The effects of material properties on bond strength between reinforcing bar, concrete exposed to high temperature. *Constr. Build. Mater.* **2016**, *112*, 691–698. [CrossRef]
55. Li, G.Q.; Jiang, S.C.; Yin, Y.Z.; Chen, K.; Li, M.F. Experimental studies on the properties of constructional steel at elevated temperatures. *J. Struct. Eng.* **2003**, *129*, 1717–1721. [CrossRef]
56. Miamis, K. A Study of the Effects of High Temperature on Structural Steel Framing. Ph.D. Thesis, Purdue University, West Lafayette, Indiana, 2007.
57. Kwon, I.; Shin, S. Mechanical thermal properties of SM 490 at high temperature for fire engineering design. *Met. Mater. Int.* **2010**, *16*, 559–564. [CrossRef]
58. Santiago, A.; Silva, L.S.D.; Real, P.V.; Vaz, G.; Lopes, A.G. Experimental evaluation of the influence of connection typology on the behavior of steel structures under fire. *Eng. J.* **2009**, *46*, 81–98.
59. Kirby, B.R. The behaviour of high-strength grade 8.8 bolts in fire. *J. Constr. Steel Res.* **1995**, *33*, 3–38. [CrossRef]
60. Banea, M.D.; de Sousa, F.; da Silva, L.; Campilho, R.; de Pereira, A.B. Effects of temperature and loading rate on the mechanical properties of a high temperature epoxy adhesive. *J. Adhes. Sci. Technol.* **2011**, *25*, 2461–2474. [CrossRef]

61. Li, Z.J.; Chau, C.K. Influence of molar ratios on properties of magnesium oxychloride cement. *Cem. Concr. Res.* **2007**, *37*, 866–870. [CrossRef]
62. Alley, R.I.; Caine, G.E. Magnesium Oxychloride Cement Compositions and Methods for Manufacture and Use. U.S. Patent 5,004,505, 2 April 1991.
63. Malinowski, S.; Jaroszyńskawolińska, J. The physical and mechanical properties of magnesium oxychloride cement-based materials. *Bud. I Archit.* **2015**, *14*, 89–98.
64. Wu, J.Y.; Zhu, S.Q. The development of magnesium oxychloride cement and its products. *China Non-Met. Min. Ind. Her.* **2006**, *1*, 3.

© 2019 by the authors. Licensee MDPI, Basel, Switzerland. This article is an open access article distributed under the terms and conditions of the Creative Commons Attribution (CC BY) license (http://creativecommons.org/licenses/by/4.0/).